

Gold nanoparticles conjugated with DNA aptamer for photoacoustic detection of human matrix metalloproteinase-9

Jinhwan Kim ^{a,b}, Anthony M. Yu ^a, Kelsey P. Kubelick ^{a,b}, Stanislav Y. Emelianov ^{a,b,*}

^a Wallace H. Coulter Department of Biomedical Engineering, Georgia Institute of Technology and Emory University School of Medicine, Atlanta, GA 30332, USA

^b School of Electrical and Computer Engineering, Georgia Institute of Technology, Atlanta, GA 30332, USA

ARTICLE INFO

Keywords:

Photoacoustic imaging
Gold nanoparticles
Nanosensors
DNA aptamers
Matrix metalloproteinase-9

ABSTRACT

Matrix metalloproteinase-9 (MMP-9) plays major roles in extracellular matrix (ECM) remodeling and membrane protein cleavage, suggesting a high correlation with cancer cell invasion and tumor metastasis. Here, we present a contrast agent based on a DNA aptamer that can selectively target human MMP-9 in the tumor microenvironment (TME) with high affinity and sensitivity. Surface modification of plasmonic gold nanospheres with the MMP-9 aptamer and its complementary sequences allows the nanospheres to aggregate in the presence of human MMP-9 through DNA displacement and hybridization. Aggregation of gold nanospheres enhances the optical absorption in the first near-infrared window (NIR-I) due to the plasmon coupling effect, thereby allowing us to detect the aggregated gold nanospheres within the TME via ultrasound-guided photoacoustic (US/PA) imaging. Selective and sensitive detection of human MMP-9 via US/PA imaging is demonstrated in solution of nanosensors with the pre-treatment of human MMP-9, *in vitro* in cell culture, and *in vivo* in a xenograft murine model of human breast cancer.

1. Introduction

Matrix metalloproteinases (MMPs) are a family of zinc-dependent endopeptidases, which have specific proteolytic activity towards several substrates within the extracellular matrix (ECM) [1,2]. In particular, MMP-9 plays significant roles in ECM remodeling and membrane protein cleavage, suggesting a close association between MMP-9 and cancer pathologies including cancer cell invasion and metastasis [3]. Due to this relationship, MMP-9 is a good biological target molecule for detection or inactivation of cancer cells [4–6]. However, because of the structural and functional similarity within the MMP family of proteins, it has been quite challenging to detect/target MMP-9 with high selectivity and sensitivity, especially in complex *in vivo* environments [7].

Molecular photoacoustic (PA) imaging, a noninvasive imaging modality that leverages thermoelastic expansion caused by light absorption, has shown great potential in biomedical and clinical imaging applications [8,9]. PA imaging is highly advantageous under the guidance of ultrasound (US) imaging. Ultrasound provides excellent anatomical images of tissue with high spatial resolution, while complementary PA imaging can convey functional information with high

contrast, resolution, imaging depth, and sensitivity [10]. Although endogenous contrast from tissue can produce PA signal, the use of an exogenous contrast agent can significantly enhance PA signal, allowing for better imaging of cellular and molecular events [11]. For example, a contrast agent that changes its optical absorption in response to a specific stimulus can be exploited as a PA-based biosensor for longitudinal detection *in vivo* [12]. PA imaging contrast depends on having distinct optical signatures between the imaging contrast agent and the background tissue; therefore, an optimal exogenous contrast agent should absorb at wavelengths where absorption of biological tissues is minimal.

Gold nanoparticles (AuNPs), such as gold nanospheres (AuNSs) and gold nanorods (AuNRs), have been widely utilized as PA contrast agents because of their strong, tunable optical absorption [13–15]. Size-dependent localized surface plasmon resonance (LSPR) of AuNPs has been exploited to create contrast agents with an optimal absorbance range for the desired application [16–18]. The size-dependent absorption shift occurs when the AuNPs are interacting close enough to one another (within 10 nm) such that the surface electrons overlap, also known as the plasmon coupling effect [19–21]. This plasmon coupling opens the potential to use AuNPs as a biosensor by controlling their dynamic assembly/disassembly in response to a specific

* Correspondence to: School of Electrical & Computer Engineering, and Wallace H. Coulter Department of Biomedical Engineering, Georgia Institute of Technology and Emory University School of Medicine, Atlanta, GA 30332, USA.

E-mail address: stas@gatech.edu (S.Y. Emelianov).

microenvironment or to the existence of a target biomolecule. For a plasmon coupling strategy, AuNSs are advantageous over other Au-based nanomaterials including AuNRs and Au nanostars. The optical absorption range of 650–900 nm, known as the first near infrared (NIR-I) window, is important for PA imaging as there is relatively low background optical absorption from tissue and high imaging penetration depth at these wavelengths. When AuNSs are singular and monodisperse particles, their maximum optical absorption is around 520 nm, with very low optical absorption from 650 to 900 nm. However, the optical absorption spectrum of the AuNSs redshifts and broadens upon aggregation. As a result, the optical absorption from 650 to 900 nm increases significantly for aggregated nanospheres compared to singular AuNSs. Therefore, AuNSs produce nearly on/off changes in the NIR-I window upon their assembly, enabling them to serve as PA nanosensors. Researchers have leveraged various functional moieties that trigger the assembly/aggregation and disassembly based on charge conversion [22], changes in hydrophilicity/hydrophobicity balance [23], host-guest interaction [24], and DNA hybridization [25–27].

Exploiting DNA hybridization provides several advantages such as programmability, predictability, and biocompatibility [28]. In particular, oligomeric DNA sequences can be designed to transform their structures in response to a specific stimulus, such as pH or biomolecules, rather than forming a sequence-specific double-strand with their complementary sequence [29,30]. DNA aptamers, oligonucleotides that bind to a specific target molecule, represent one class of functional oligomeric DNA sequences [31]. DNA aptamers are advantageous due to their ability to bind to specific target molecules with high affinity, selectivity, and specificity [32]. In this regard, we can design a double-strand of a DNA aptamer and its complementary sequence, which forms regular hydrogen bonds (Watson-Crick base pairing) in the absence of a target protein. In the presence of a target protein however, the DNA aptamer releases its complementary sequence to instead bind with the target protein, which is a more favorable interaction. Thus, the

DNA aptamer can detect and silence target biomolecules through dynamic DNA displacement.

Here we report a PA contrast agent as a biosensor for the detection of human MMP-9 (hMMP-9) by introducing programmed hybridization/dehybridization of DNA aptamers on the surface of AuNSs. To develop the sensor, the surface of 15 nm-sized AuNSs was modified with two different sets of DNA strands to create AuNS-1 and AuNS-2, respectively. For AuNS-1, double strands of hMMP-9 aptamer and its partial complementary sequence (comp-1) were grafted on the surface of AuNSs. To create AuNS-2, single stranded, full-match complementary sequences of comp-1 (comp-2) were conjugated on the surface. In the absence of MMP-9, the binding of comp-2 to comp-1 is blocked by pre-bound MMP-9 aptamers, maintaining the LSPR of 15 nm-sized AuNSs (a mixture of single nanospheres of AuNS-1 and AuNS-2). However, in the presence of hMMP-9, the MMP-9 aptamer DNA strand preferentially binds to the hMMP-9 protein instead of binding to the comp-1 to form the MMP-9-aptamer complex. The release of the MMP-9 aptamer sequence from AuNS-1 then enables the binding of comp-2 on AuNS-2 to comp-1 on AuNS-1, coupling AuNS-1 and AuNS-2 (Fig. 1a). The coupling of AuNS-1 and AuNS-2 results in the aggregation of the AuNSs, inducing the LSPR changes. The hMMP-9-responsive aggregation and consequent optical absorption shift were detected by US-guided spectroscopic PA (sPA) imaging. A series of proof-of-concept studies of our sensor were carried out in solution of nanosensors with the pre-treatment of hMMP-9, *in vitro* in cell culture, and *in vivo* in a murine xenograft model of human breast cancer (Fig. 1b).

2. Materials and methods

2.1. Materials

Gold chloride hydrate (HAuCl_4), sodium citrate tribasic dihydrate, tris(2-carboxyethyl)phosphine hydrochloride (TCEP), sodium chloride

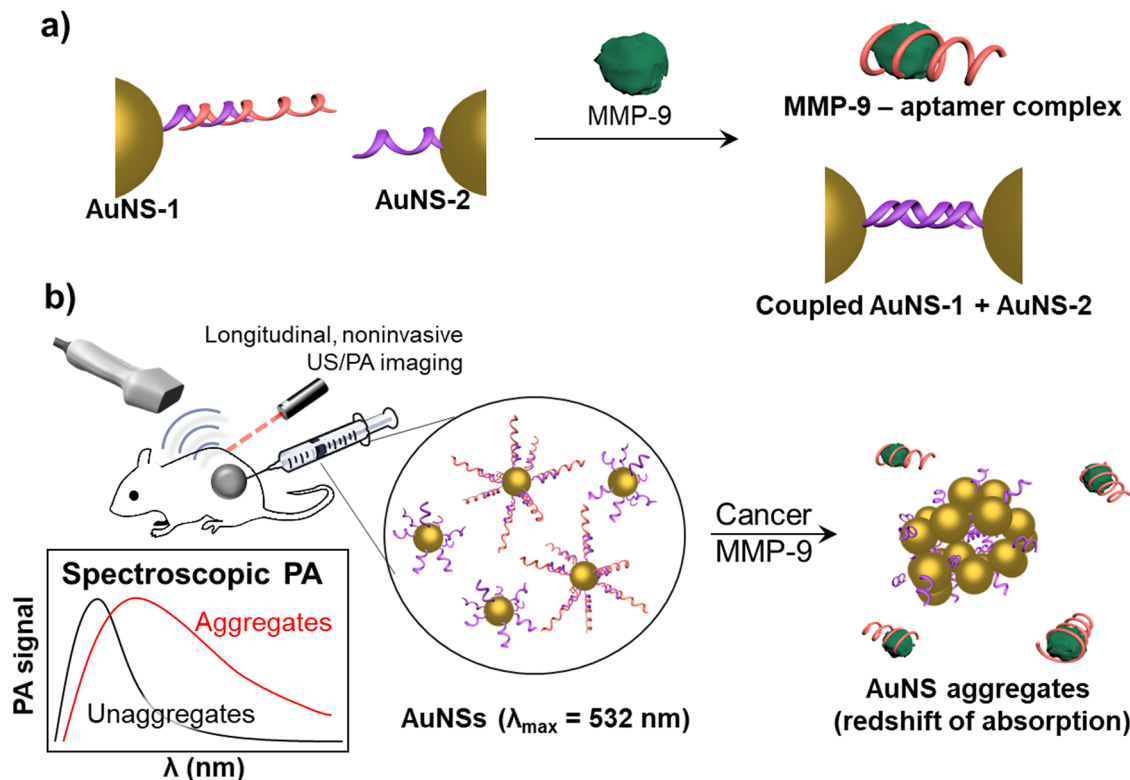


Fig. 1. Schematic illustration of a contrast agent for the detection of human matrix metalloproteinase-9 (hMMP-9). (a) Design of a plasmon coupling-based MMP sensor induced by the DNA displacement in the presence of the MMP-9. (b) Detection of the MMP-9 in the tumor microenvironment using the ultrasound-guided spectroscopic PA (US/sPA) imaging.

(NaCl), magnesium chloride ($MgCl_2$), tris base, and potassium cyanide (KCN) were purchased from Sigma-Aldrich (St. Louis, MO) and used as received without further purification or modification. All oligonucleotide sequences were purified by standard desalting and purchased from IDT Inc. (Coralville, IA). The sequences of the DNA strands are the following: MMP-9 aptamer, 5'-TCG TAT GGC ACG GGG TTG GTG TTG GGT TGG -3' [33]; comp-1 of MMP-9 aptamer, 5'-GGT GTG CCA TAC GAA A/3ThioMC3-D/-3'; comp-2 of MMP-9 aptamer, 5'-TCG TAT GGC ACA CCA A/3ThioMC3-D/-3'; control aptamer, 5'-CCG GTG TTC GAG ACA AGA GTC CAG GG -3'; comp-1 of control aptamer, 5'-CTC TCG AAC ACC GGA A/3ThioMC3-D/-3'; comp-2 of control aptamer, 5'-CCG GTG TTC GAG AGA A/3ThioMC3-D/-3', where /3ThioMC3-D/ stands for 3-(butyldisulfanetyl)propan-1-ol to provide a disulfide structure at the 3' end of the DNA strands. Human recombinant MMP-9 and MMP-7 was purchased from BioVision (Milpitas, CA).

2.2. Synthesis of aptamer-decorated AuNSs

Synthesis of 15 nm-sized, citrate-capped AuNSs was conducted according to the previously reported method with slight modification [34]. In brief, HAuCl₄ (1.47 mM, 10 mL) and sodium citrate tribasic (0.334 M, 200 μ L) were mixed under mild stirring at 80 °C for 20 min to synthesize AuNSs. To modify the surface of citrate-capped AuNSs and create AuNS-1, the comp-1 and aptamer sequences were annealed in phosphate buffer (10 mM) containing $MgCl_2$ (1 mM) and NaCl (20 mM) to form double-strands. The annealed DNA strands were incubated in acetate buffer (pH = 5.2, 50 mM) with TCEP (1 mM) for 1 h to activate the thiol group. The aptamer/comp-1 duplexes were then added dropwise to 7 nM citrate capped AuNSs with a ratio of 1:50 (AuNS:duplex), followed by salt aging for 24 h. To create AuNS-2, the thiol groups in comp-2 single strands were activated as described for aptamer/comp-1 duplexes, then added dropwise to 7 nM citrate capped AuNSs with a molar ratio of 1:100 (AuNS:single strand), followed by salt aging for 24 h. The final AuNS-1 and AuNS-2 were purified by centrifugation (16,100 rcf, 30 min) with tris-acetate buffer (pH = 8.2, 25 mM) and NaCl (0.1 M).

2.3. Aggregation monitoring of AuNSs with the pre-treatment of hMMP-9

The mixture solution of AuNS-1 and AuNS-2 (1:1 ratio, 5 nM of Au in 200 μ L of 25 mM tris-acetate buffer) was incubated at 37 °C in a humidified incubator with the hMMP-9 stock solution to reach a final hMMP-9 concentration of 0.04–5 μ g/mL (1.03–128 nM of hMMP-9). After 24 h incubation, the optical absorption spectra were measured with a UV-vis spectrophotometer (Evolution 220, Thermo Scientific), the hydrodynamic size was checked with a Dynamic Light Scattering instrument (Zetasizer Nano ZS, Malvern Instruments Ltd.), and the size and morphology were characterized with transmission electron microscopy (TEM) (HT7700, Hitachi).

2.4. Phantom preparation and US/sPA imaging

The tube phantom was prepared by adding 40 μ L of the MMP sensor solution (2.5 nM of AuNS-1 and AuNS-2) with MMP-9, BSA, and MMP-7 (2.5 μ g/mL each, 64 nM of hMMP-9) into polyethylene tubes held in 3D-printed housing. The prepared phantom was imaged using the Vevo2100/LAZR imaging system (FujiFilm VisualSonics, Inc.). US/sPA images were acquired using an LZ250 transducer, which is a 256-element ultrasound transducer array operating at 18.5 MHz center frequency. The LAZR (laser source) is a Q-switched Nd:YAG pumped optical parametric oscillator (OPO) laser (pulse duration = 7 ns; frame rate = 5 Hz). For spectroscopic PA analysis, the phantom was imaged using wavelengths from 680 to 970 nm in 2 nm intervals. The representative tube phantom image was acquired at 700 nm with 3D mode, followed by image reconstitution using maximum intensity projection (MIP) in VevoLAB 2.2 software (FujiFilm Visualsonics, Inc.). The gelatin phantom's base consisted of 8% gelatin and 0.2% silica (0.25 μ m

diameter). The inclusions were prepared by mixing the MMP sensor at different conditions with the same volume of heated 16% gelatin solution. The prepared inclusions were loaded on the phantom base to create dome-shaped phantoms for imaging with the same Vevo2100/LAZR imaging system. Each dome-shaped inclusion was imaged using wavelengths from 680 to 970 nm in 2 nm intervals. All data was exported and processed in VevoLAB 2.2 software and post-processed in MATLAB (MathWorks, Inc.).

2.5. Cell culture

MDA-MB-231 human breast adenocarcinoma cells were cultured in Dulbecco's Modified Eagle's Medium (DMEM, Corning) supplemented with 10% fetal bovine serum (FBS, Corning), 100 I.U./mL penicillin and 100 μ g/mL streptomycin. Cells were incubated at 37 °C in a 5% CO₂ humidified incubator.

2.6. In vitro toxicity test

MDA-MB-231 cells in culture medium were seeded in a 96-well plate at an initial density of 8 × 10³ cells/well and incubated at 37 °C in a 5% CO₂ humidified incubator overnight. The next day, the MMP sensor was added to cells to yield a final concentration of 0.3125, 0.625, 1.25, 2.5, 5, and 10 nM in solution. One group contained no MMP and received PBS as a control. Cells were then further incubated for 24 h, followed by washing with PBS three times to remove nanoparticles prior to the viability assay. Culture medium with 0.5 mg/mL of 3-(4,5-Dimethylthiazol-2-yl)-2,5-Diphenyltetrazolium Bromide (MTT) was added to each well. After 4 h, the solution was removed and the formazan salt on the bottom of the well plate was dissolved by adding 200 μ L of DMSO. The absorbance at 590 nm was measured using a multi-well plate reader (Synergy HT, BioTek), with the cells treated with PBS considered as 100% viable.

2.7. In vitro transwell study

MDA-MB-231 cells were cultured in phenol red-free medium and were seeded on the upper compartment of a transwell insert (12 mm transwell with a polyester membrane, pore size = 0.4 μ m) at an initial density of 2 × 10⁵ cells/insert and incubated at 37 °C in a 5% CO₂ humidified incubator overnight. Then, 10 μ L of 100 μ g/mL phorbol 12-myristate 13-acetate (PMA) in DMSO were added on the upper compartment of the transwell insert and further incubated for 24 h. After 24 h, the lower compartment of the 12-well plate was filled with phenol red-free culture media containing 2.5 nM of MMP sensor and its derivatives. The solution (100 μ L) in the lower compartment was collected at different time points (initial, 1, 4, 12, 24 h) and concentrated to the final volume of 40 μ L, followed by the preparation of dome-shaped 8% gelatin inclusions as described above. The inclusions were imaged using the aforementioned Vevo2100/LAZR imaging system with the same protocol.

2.8. In vivo imaging

All animal procedures were approved by the Institutional Animal Care and Use Committee (IACUC) at Georgia Institute of Technology and were performed in accordance with the federal guidelines for the care and use of laboratory animals. MDA-MB-231 cells were inoculated subcutaneously (s.c.) into the flank of 6-week-old female NU/NU mice (Charles River) at an initial density of 1 × 10⁷ cells in 50% Matrigel (Corning). After the average tumor volume reached over 100 mm³, 200 μ L of 500 μ g/mL PMA in 10% DMSO were injected intraperitoneally 48 h before imaging according to previously established methods [35]. After 24 h, the MMP sensor/control sensor (same quantity of AuNS-1 and AuNS-2 mixture at OD = 5, 100 μ L) was injected peritumorally. US/sPA imaging was performed after another 24 h, where the mice were

anesthetized and placed on a heated translational motor stage. *In vivo* images were acquired with a 40 MHz ultrasound transducer (LZ-550) coupled with a fiber optic bundle for photoacoustic imaging. All data was exported using the VevoLAB 2.2 software (FujiFilm Visual Sonics, Inc.) and post-processed in MATLAB (MathWorks, Inc.). Photoacoustic spectra were corrected for wavelength-dependent laser energy fluctuation using local background signal outside the tissue boundary. Photoacoustic images were median filtered to remove large spikes and mean filtered to smooth before being spectroscopically analyzed over the entire OPO wavelength range of 680–970 nm.

2.9. Photoacoustic tomography

All photoacoustic tomography images were collected using the TriTom system (Photosound Technologies, Inc.), a photoacoustic-fluorescence tomography (PAFT) 3D imaging system. The TriTom system was paired with the Phocus Mobile HE laser system (Opotek, Inc.) for OPO operation, which produces a 690–950 nm 10 Hz pulsed output pumped by a 1064 nm Nd:YAG laser. For 532 nm operation, the TriTom system was paired with a Vibrant 532-I (Opotek, Inc.), another 10 Hz pulsed Nd:YAG laser which produces 532 nm output from its second harmonic generator. Excitation laser beams are directed to the imaging chamber using multi-output randomized fiber bundles. Mice are immersed in a heated water bath within a glass imaging tank, with oxygen and inhalable anesthesia available for *in vivo* imaging. Data is acquired by rotating the target within the FOV of a curved array transducer, generating a spherical sensor map. Image reconstruction was performed using Photosound software, and volume visualization was performed using 3D Slicer, a free open-source image processing software.

3. Results

Prior to modifying DNA sequences on the AuNSs, the hybridization

of each strand was confirmed by 15% polyacrylamide gel electrophoresis (PAGE). The addition of the comp-2 sequence to the pre-formed duplex of aptamer-comp-1 did not displace the original hybridization between the aptamer and comp-1. Meanwhile, the addition of comp-2 in the absence of the aptamer successfully created double-stranded DNA (Fig. S1). This result suggests the formation of the MMP-9-aptamer complex and the exposure of the comp-1 sequence would allow the aggregation of AuNS-1 and AuNS-2 via sequence-specific hybridization. With that, the surface of the 15-nm AuNSs was modified with hMMP aptamer-comp-1 duplexes (AuNS-1) or comp-2 single strands (AuNS-2) by a salt aging process reported elsewhere [36]. AuNS-1 and AuNS-2 for the MMP sensor contain ~26 double-strands and ~38 single strands, respectively. The surface modification of AuNSs did not show a remarkable absorption shift or aggregation in the UV-vis spectrum and transmission electron microscopy (TEM) analysis (Fig. S2). Similarly, we designed and characterized a control MMP sensor with random DNA sequences (see experimental section for detailed DNA sequences), which did not respond to hMMP-9, to compare the responsiveness to the experimental MMP sensor (Fig. S3).

We then confirmed the assembly of the MMP sensor (5 nM of AuNS-1 and AuNS-2) in response to the target protein (5 µg/mL or 128 nM of hMMP-9) by co-incubating them in buffer solution for 24 h. In colorimetric monitoring, without hMMP-9 (incubation with buffer) or with the addition of random protein (bovine serum albumin, BSA), the color of the sensor solution did not change, indicating there was no plasmon coupling. In contrast, the solution containing both the MMP sensor and hMMP-9 changed color, due to the plasmon coupling induced by the MMP-9-aptamer complex formation and subsequent binding of comp-1 and comp-2 (Fig. 2a). The UV-vis spectra further confirmed the red-shift of the MMP sensor only in the case of incubation with the target protein, hMMP-9 (Fig. 2b). Furthermore, we tested the optical absorption shift as the concentration of hMMP-9 ranged from 0.04 to 5 µg/mL (1.03–128 nM), which demonstrated that a higher concentration of hMMP-9 induced more aggregation of AuNSs (Fig. S4). In addition, the

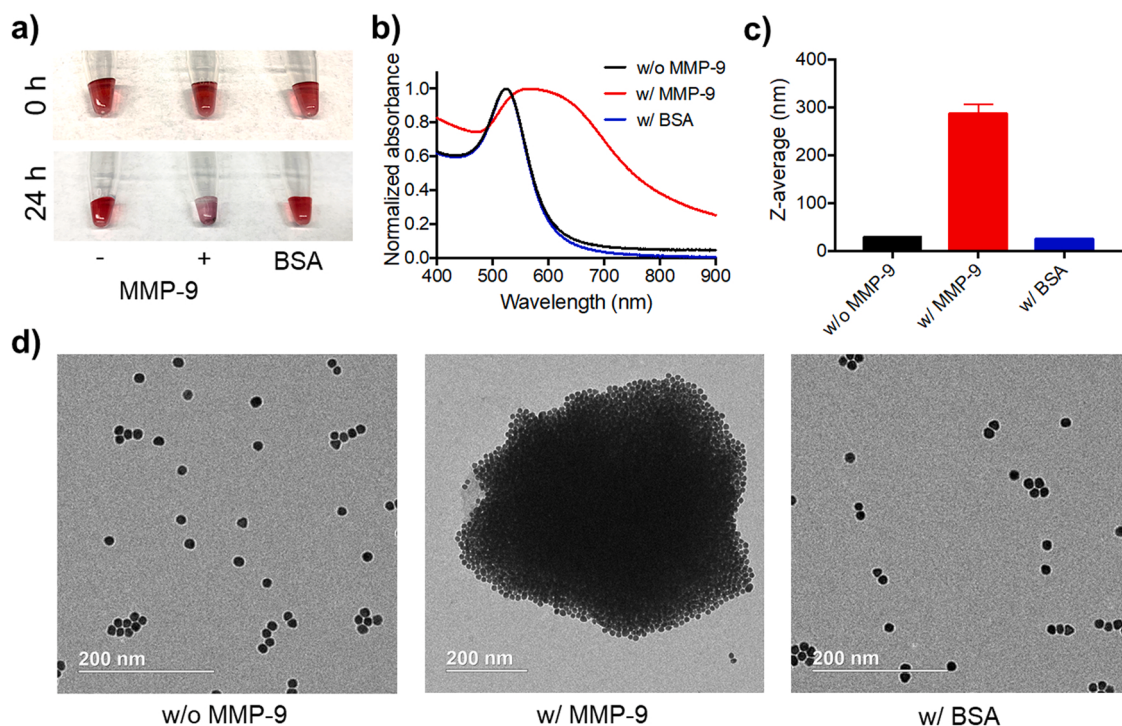


Fig. 2. MMP-9-responsive aggregation of gold nanospheres (AuNSs). (a) Color changes of the MMP sensor without hMMP-9, with hMMP-9, and with bovine serum albumin (BSA) before (0 h, upper image) and after 24 h (lower image). (b) UV-vis spectra and (c) hydrodynamic size of the MMP sensor without hMMP-9, with hMMP-9, and with BSA after 24 h. (d) Transmission electron microscopy (TEM) images of the MMP sensor without hMMP-9 (left), with hMMP-9 (middle), and with BSA (right). Scale bar = 200 nm. (For interpretation of the references to color in this figure legend, the reader is referred to the web version of this article.)

selective aggregation of the MMP sensor to hMMP-9 was monitored by measuring size with dynamic light scattering (DLS) and TEM. Without hMMP-9 or when co-incubated with a control protein, the sensor did not change in size or morphology (Fig. 2c and d). These results support our sensor's potential as a PA imaging agent.

To evaluate the potential of our MMP sensor in sPA imaging, we prepared the MMP sensor (2.5 nM of AuNS-1 and AuNS-2) with BSA, hMMP-7, and hMMP-9 (2.5 µg/mL respectively) in a polyethylene (PE) tube phantom and subsequently imaged the phantom using the Vevo 2100/LAZR imaging system. Qualitatively, our MMP sensor pre-treated with hMMP-9 showed a strong PA signal at 700 nm compared to signals from the sensor incubated with BSA or hMMP-7 (Fig. 3a). The representative PA spectrum of the MMP sensor with hMMP-9 showed a 10-fold higher PA signal at 700 nm than the MMP sensor with BSA or hMMP-7 (Fig. 3b), demonstrating the selectivity of our MMP sensor towards hMMP-9. We further imaged the MMP sensor with/without hMMP-9 in a thin polytetrafluoroethylene (PTFE) tube phantom using a photoacoustic tomography (PAT) imaging system (TriTom, PST Inc.) at 532 nm and from 680 to 970 nm (Fig. S5). PAT phantom studies further corroborated previous UV-vis (Fig. 2b) and PA results from the Vevo 2100/LAZR (Fig. 3). Similarly, the MMP sensor with hMMP-9 in the PAT phantom exhibited a stronger PA signal from 680 to 970 nm and a weaker PA signal at 532 nm compared to controls (no hMMP-9 or with control protein, BSA). It is worth noting that the wavelengths ranging from 650 to 900 nm are in the NIR-I window where light has its maximum penetration depth and relatively low background optical absorption in tissue. Therefore, our MMP sensor, exhibiting strong PA signal over the wavelength range of 680–970 nm, offers huge potential for more complex *in vivo* detection of hMMP-9, with enhanced optical absorption at ideal wavelengths in response to the target protein.

Next, we tested *in vitro* hMMP-9 detection secreted from MDA-MB-231 human breast cancer cells. MDA-MB-231 cells were seeded on the semi-permeable membrane of the upper insert of a transwell plate. MMP sensors suspended in cell culture medium were incubated in the lower compartment of the transwell to detect secreted hMMP-9. The MMP sensor-containing media was collected at different time intervals and embedded in a dome-shaped 8% gelatin phantom to monitor our sensor's longitudinal behavior in US/sPA imaging (Fig. 4a). PA signals at 680–970 nm were gradually enhanced until 24 h as higher amounts of hMMP-9 were transferred from cells to the lower compartment with increasing incubation time, demonstrating the quantitative detection of hMMP-9 (Fig. 4b and c). In contrast, when we replaced the MMP sensor at the lower transwell compartment with the control sensor decorated with random/scrambled DNA sequences (Fig. S3), the PA images at the 680–970 nm did not exhibit any distinct signal (Fig. S6). Furthermore, the UV-vis spectrum of the MMP sensor in the culture medium or of the

control sensor in the medium were well-correlated with the corresponding PA spectrum (Fig. S7). In addition, MDA-MB-231 cells treated with the MMP sensor did not exhibit noticeable toxicity up to 10 nM while only 2.5 nM of our MMP sensor was needed for the detection of hMMP-9, reducing the toxicity concerns of our MMP sensor (Fig. S8). Together, these results show successful demonstration of our MMP sensor for the selective detection of hMMP-9 at the cellular level by leveraging hybridization of the MMP-9 aptamer and related DNA sequences.

Finally, we detected hMMP-9 *in vivo* using our MMP sensor as a contrast agent for US/sPA imaging and PAT in a xenograft mouse model of breast cancer (MDA-MB-231). For US/sPA imaging using the Vevo 2100/LAZR system, mice were subcutaneously injected with MDA-MB-231 cells. Tumors continued to grow over a period of 6 weeks until the size was over 100 mm³. The mice were injected with the MMP sensor and two controls, saline only and the control sensor, 24 h before imaging. Multiwavelength photoacoustic datasets were acquired under ultrasound guidance. The saline control and control sensor showed minimal PA signal. The PA spectrum of the MMP sensor *in vivo* closely matched *in vitro* results. Both showed a maximum PA signal at 710 nm (Fig. 4c), likely resulting from the aggregation of AuNS-1 and AuNS-2 upon formation of the MMP-9-aptamer complex (Fig. 5a). To visualize the distribution and detectability of the MMP sensors volumetrically, the TriTom system was used to perform photoacoustic tomography, generating 3-dimensional maps of the skin and surface vasculature (532 nm, yellow) and the aggregated AuNSs (710 nm, red) upon the peritumoral injection of the saline only, control sensor, and MMP sensor (Fig. 5b). In the mice injected with saline (Movie S1) or control sensor (Movie S2), signals from surface vasculature (532 nm) were observed, while the signal from aggregated AuNSs (710 nm) was not detected at the tumor periphery, indicated by the light blue circle. However, the aggregated MMP sensor was clearly detected using PAT, with a majority of the 710 nm signal distributed in the tumor (Movie S3). The results from both the Vevo LAZR and TriTom imaging systems illustrates the feasibility of the developed sensor as a contrast agent for detection of hMMP-9 *in vivo* via molecular PA imaging.

Supplementary material related to this article can be found online at doi:10.1016/j.pacs.2021.100307.

4. Discussion

In the current study, we demonstrated functional oligomeric DNA-modified AuNSs for detecting hMMP-9 *in vivo*. The use of DNA aptamers for AuNS-based nanosensors enabled sensitive and selective detection of hMMP-9. Controlling the assembly of AuNSs and their plasmon coupling based on DNA strand displacement was a unique approach to

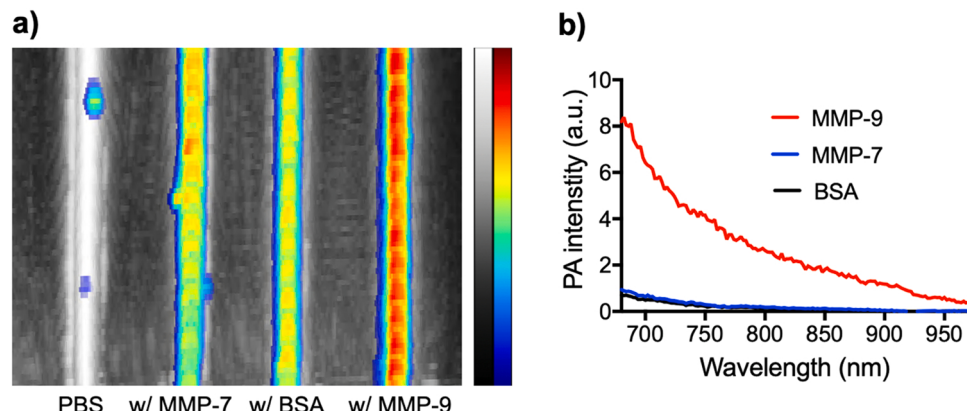


Fig. 3. Spectroscopic PA imaging of the MMP sensor 24 h after the pre-treatment with hMMP-9 and assorted controls. (a) Maximum intensity projection (MIP)-reconstituted US/PA overlay image at 700 nm of PBS and the MMP sensor (2.5 nM of AuNS-1 and AuNS-2) with hMMP-9, hMMP-7, and BSA (2.5 µg/mL) in a tube phantom. (b) PA intensity of the MMP sensor at 680–970 nm.

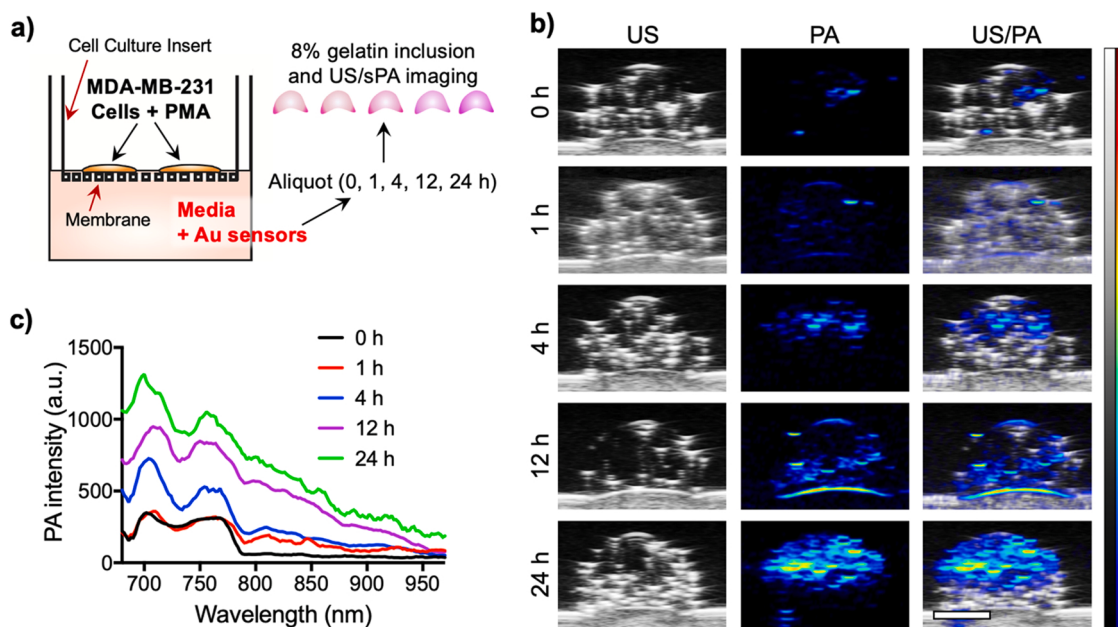


Fig. 4. Time-dependent spectroscopic PA imaging in a transwell. (a) Schematic illustration of the experimental setup. (b) US, PA, and overlay image of the MMP sensor in the lower compartment of the transwell at 0, 1, 4, 12, 24 h after incubation. Scale bar = 2 mm. (c) Incubation time-dependent PA intensity of the MMP sensor at 680–970 nm.

create distinct spectral signatures for spectroscopic PA imaging. Moreover, the scrambled sequence-modified AuNSs (control sensor) did not exhibit random aggregation *in vitro* or *in vivo*, demonstrating the stability of oligomeric DNA-modified AuNSs in a biological microenvironment. Furthermore, binding of the target biomolecule with the DNA aptamer is highly sequence-dependent. In the future, introducing a set of orthogonal aptamers that target different biomolecules can allow multiplex US/PA imaging to monitor the biomolecular profile of a microenvironment. Thus, programmable design of DNA sequences and strategic selection of the DNA aptamer allows almost infinite combinations for biomolecule detection to develop a robust US/PA imaging platform.

In the complex tumor microenvironment, MMP-9 is secreted from multiple types of cells, including macrophages, fibroblasts, endothelial cells, stromal cells, and cancer cells [3]. As a model for our proof-of-concept study, we selected human breast cancer cells for the source of human MMP-9 expression. MMP-9 expression is regulated by cytokines and signal transduction pathways. Thus, MDA-MB-231 human breast cancer cells required pre-treatment with PMA *in vitro* and *in vivo* to activate the NF- κ B pathway that secretes hMMP-9 as confirmed by an ELISA of hMMP-9 (Fig. S9a). Without a stimulus for pathway activation, MDA-MB-231 cancer cells themselves produce negligible amounts of hMMP-9 in xenograft models [37]. Therefore, to validate our model system, we compared the PA signal of the MMP sensor with and without pre-treating MDA-MB-231 cells with PMA. Without PMA pre-treatment, the PA signal from the MMP sensor was negligible over the entire OPO wavelength range of 680–970 nm, confirming that PMA is required in our model system (Fig. S9b–d). Moreover, this result further supports our main hypothesis that the secreted hMMP-9 from the cells triggers the aggregation by forming an MMP-9–aptamer complex. From a translational perspective, pretreatment with PMA would not be required. Unlike the xenograft model, the secretion of hMMP-9 in humans will be orchestrated by multiple cell types, including macrophages, fibroblasts, endothelial cells, stromal cells, and cancer cells at the tumor site [3]. Therefore, hMMP-9 can be produced endogenously with no further stimulation.

Previous studies of *in vivo* MMP or protease sensors employed the catalytic activity of MMPs to cleave a specific chemical bond or degrade

polymer structure for detection [38–41]. In the current study, the MMP sensor is based on structural one-to-one binding of the hMMP-9 protein to the DNA aptamer. This protein binding to the DNA aptamer could be applied not only for the detection of the target protein, as we demonstrated here, but also for the selective capture and deactivation of the target protein. Selective capture and deactivation of disease-related pathogenic proteins at the disease site can impact disease progression. In this case, hMMP-9 is highly related to ECM remodeling and cancer progression. Our MMP sensor can serve as a theranostic agent by detecting and deactivating hMMP-9 through selective capture with DNA aptamers, which may inhibit tumor growth by preventing ECM remodeling.

5. Conclusions

In summary, we have developed a PA biosensor to detect hMMP-9 by exploiting plasmonic AuNSs and DNA aptamers. The use of DNA aptamers enabled sensitive and selective detection of hMMP-9, while the plasmon coupling between AuNSs by programmable DNA hybridization resulted in selective PA signal amplification in the NIR-I optical window. Moreover, the versatility and customizability of oligomeric DNA sequences will enable the design of other AuNS-based sensors for the detection and capture of biomolecules by utilizing the corresponding aptamer sequence. By incorporating multiple aptamers that target different biomolecules on the nanoparticles, our approach provides unlimited opportunities to develop contrast agents for multiplex imaging of biomolecules.

Funding

This work was supported by the Breast Cancer Research Foundation (BCRF-20-043) and the National Institute of Health (EB015007, EY030071, NS102860, NS117613).

Declaration of Competing Interest

The authors declare that they have no known competing financial interests or personal relationships that could have appeared to influence

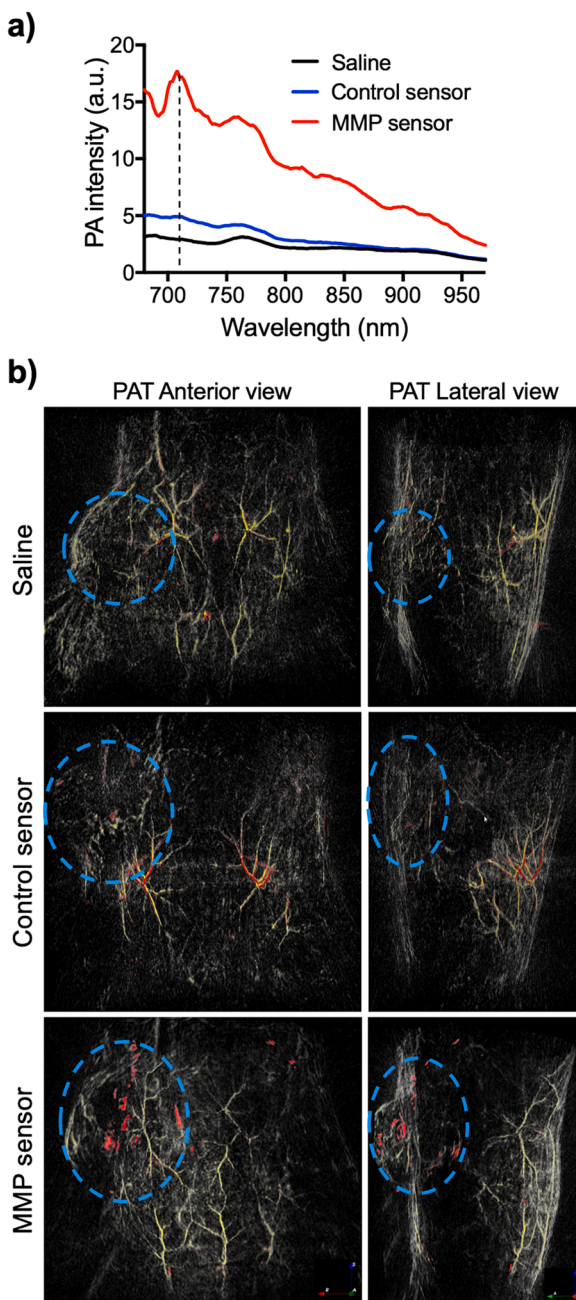


Fig. 5. Spectroscopic analysis and PAT of the MMP sensor in an *in vivo* mouse model of breast cancer. (a) PA intensity from 680 nm to 970 nm of the MMP sensor in the tumor region and assorted controls – saline only and control sensor. Black dashed line marks 710 nm. (b) Overlaid photoacoustic tomography of saline, control sensor, and MMP sensor-injected mice. The volumes of skin and surface vasculature (532 nm) are colored in yellow and aggregated nanoparticles (710 nm) are colored in red, with the light blue dashed line indicating the tumor boundary. (For interpretation of the references to color in this figure legend, the reader is referred to the web version of this article.)

the work reported in this paper.

Acknowledgments

We acknowledge Dr. Younan Xia and Ruhui Chen of Georgia Institute of Technology for assistance with UV-vis spectrophotometer measurements and Anamik Jhunjhunwala of Georgia Institute of Technology for helping with tube phantom imaging.

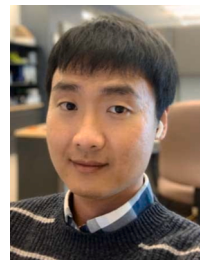
Appendix A. Supporting information

Supplementary data associated with this article can be found in the online version at doi:10.1016/j.pacs.2021.100307.

References

- [1] C.E. Brinckerhoff, L.M. Matisian, Timeline – matrix metalloproteinases: a tail of a frog that became a prince, *Nat. Rev. Mol. Cell Biol.* 3 (3) (2002) 207–214.
- [2] A. Page-McCaw, A.J. Ewald, Z. Werb, Matrix metalloproteinases and the regulation of tissue remodelling, *Nat. Rev. Mol. Cell Biol.* 8 (3) (2007) 221–233.
- [3] H. Huang, Matrix Metalloproteinase-9 (MMP-9) as a Cancer Biomarker and MMP-9 Biosensors: recent advances, *Sensors* 18 (10) (2018) 3249.
- [4] J. Cathcart, A. Pulkoski-Gross, J. Cao, Targeting matrix metalloproteinases in cancer: bringing new life to old ideas, *Genes Dis.* 2 (1) (2015) 26–34.
- [5] A. Winer, S. Adams, P. Mignatti, Matrix metalloproteinase inhibitors in cancer therapy: turning past failures into future successes, *Mol. Cancer Ther.* 17 (6) (2018) 1147–1155.
- [6] H.C. Schunk, D.S. Hernandez, M.J. Austin, K.S. Dhada, A.M. Rosales, L.J. Suggs, Assessing the range of enzymatic and oxidative tunability for biosensor design, *J. Mater. Chem. B* 8 (16) (2020) 3460–3487.
- [7] V. Lukacova, Y. Zhang, M. Mackov, P. Baricic, S. Raha, J.A. Calvo, S. Balaz, Similarity of binding sites of human matrix metalloproteinases, *J. Biol. Chem.* 279 (14) (2004) 14194–14200.
- [8] A.B.E. Attia, G. Balasundaram, M. Moothanchristos, U.S. Dinish, R. Bi, V. Ntziachristos, M. Olivo, A review of clinical photoacoustic imaging: current and future trends, *Photoacoustics* 16 (2019), 100144.
- [9] C.L. Bayer, G.P. Luke, S.Y. Emelianov, Photoacoustic imaging for medical diagnostics, *Acoust. Today* 8 (4) (2012) 15–23.
- [10] K.P. Kubelick, S.Y. Emelianov, Prussian blue nanocubes as a multimodal contrast agent for image-guided stem cell therapy of the spinal cord, *Photoacoustics* 18 (2020), 100166.
- [11] G.P. Luke, D. Yeager, S.Y. Emelianov, Biomedical applications of photoacoustic imaging with exogenous contrast agents, *Ann. Biomed. Eng.* 40 (2) (2012) 422–437.
- [12] K.S. Dhada, D.S. Hernandez, W.B. Huang, L.J. Suggs, Gold nanorods as photoacoustic nanoprobes to detect proinflammatory macrophages and inflammation, *ACS Appl. Nano Mater.* 3 (8) (2020) 7774–7780.
- [13] Y.S. Chen, Y. Zhao, S.J. Yoon, S.S. Gambhir, S. Emelianov, Miniature gold nanorods for photoacoustic molecular imaging in the second near-infrared optical window, *Nat. Nanotechnol.* 14 (5) (2019) 465–472.
- [14] P.P. Joshi, S.J. Yoon, W.G. Hardin, S. Emelianov, K.V. Sokolov, Conjugation of antibodies to gold nanorods through Fe portion: synthesis and molecular specific imaging, *Bioconjugate Chem.* 24 (6) (2013) 878–888.
- [15] W. Li, X. Chen, Gold nanoparticles for photoacoustic imaging, *Nanomedicine* 10 (2) (2015) 299–320.
- [16] J.N. Anker, W.P. Hall, O. Lyandres, N.C. Shah, J. Zhao, R.P. Van Duyne, Biosensing with plasmonic nanosensors, *Nat. Mater.* 7 (6) (2008) 442–453.
- [17] S. Mallidi, T. Larson, J. Tam, P.P. Joshi, A. Karpouli, K. Sokolov, S. Emelianov, Multiwavelength photoacoustic imaging and plasmon resonance coupling of gold nanoparticles for selective detection of cancer, *Nano Lett.* 9 (8) (2009) 2825–2831.
- [18] S.Y. Nam, L.M. Ricles, L.J. Suggs, S.Y. Emelianov, Nonlinear photoacoustic signal increase from endocytosis of gold nanoparticles, *Opt. Lett.* 37 (22) (2012) 4708–4710.
- [19] S.K. Ghosh, T. Pal, Interparticle coupling effect on the surface plasmon resonance of gold nanoparticles: From theory to applications, *Chem. Rev.* 107 (11) (2007) 4797–4862.
- [20] C. Sonnichsen, B.M. Reinhard, J. Liphardt, A.P. Alivisatos, A molecular ruler based on plasmon coupling of single gold and silver nanoparticles, *Nat. Biotechnol.* 23 (6) (2005) 741–745.
- [21] C. Tabor, D. Van Haute, M.A. El-Sayed, Effect of orientation on plasmonic coupling between gold nanorods, *ACS Nano* 3 (11) (2009) 3670–3678.
- [22] J. Nam, N. Won, H. Jin, H. Chung, S. Kim, pH-induced aggregation of gold nanoparticles for photothermal cancer therapy, *J. Am. Chem. Soc.* 131 (38) (2009) 13639–13645.
- [23] A. Sanchez-Iglesias, M. Grzelczak, T. Altantzis, B. Goris, J. Perez-Juste, S. Bals, G. Van Tendeloo, S.H. Donaldson Jr., B.F. Chmelka, J.N. Israelachvili, L.M. Liz-Marzan, Hydrophobic interactions modulate self-assembly of nanoparticles, *ACS Nano* 6 (12) (2012) 11059–11065.
- [24] Q. Zeng, R. Marthi, A. McNally, C. Dickinson, T.E. Keyes, R.J. Forster, Host-guest directed assembly of gold nanoparticle arrays, *Langmuir* 26 (2) (2010) 1325–1333.
- [25] J. Kim, C. Jo, W.G. Lim, S. Jung, Y.M. Lee, J. Lim, H. Lee, J. Lee, W.J. Kim, Programmed nanoparticle-loaded nanoparticles for deep-penetrating 3D cancer therapy, *Adv. Mater.* 30 (29) (2018), 1707557.
- [26] J. Kim, Y.M. Lee, Y. Kang, W.J. Kim, Tumor-homing, size-tunable clustered nanoparticles for anticancer therapeutics, *ACS Nano* 8 (9) (2014) 9358–9367.
- [27] H. Park, J. Kim, S. Jung, W.J. Kim, DNA-Au nanomachine equipped with i-Motif and G-Quadruplex for triple combinatorial anti-tumor therapy, *Adv. Funct. Mater.* 28 (5) (2018), 1705416.
- [28] Y.J. Chen, B. Groves, R.A. Muscat, G. Seelig, DNA nanotechnology from the test tube to the cell, *Nat. Nanotechnol.* 10 (9) (2015) 748–760.
- [29] J. Kim, D. Jang, H. Park, S. Jung, D.H. Kim, W.J. Kim, Functional-DNA-driven dynamic nanoconstructs for biomolecule capture and drug delivery, *Adv. Mater.* 30 (45) (2018), 1707351.

- [30] H. Lee, J. Kim, J. Lee, H. Park, Y. Park, S. Jung, J. Lim, H.C. Choi, W.J. Kim, In vivo self-degradable graphene nanomedicine operated by DNAzyme and photo-switch for controlled anticancer therapy, *Biomaterials* 263 (2020), 120402.
- [31] R. Stoltzenburg, C. Reinemann, B. Strehlitz, SELEX – a (r)evolutionary method to generate high-affinity nucleic acid ligands, *Biomol. Eng.* 24 (4) (2007) 381–403.
- [32] A.D. Keefe, S. Pai, A. Ellington, Aptamers as therapeutics, *Nat. Rev. Drug Discov.* 9 (7) (2010) 537–550.
- [33] S. Scarano, E. Dausse, F. Crispo, J.J. Toulme, M. Minunni, Design of a dual aptamer-based recognition strategy for human matrix metalloproteinase 9 protein by piezoelectric biosensors, *Anal. Chim. Acta* 897 (2015) 1–9.
- [34] J. Kim, J. Park, H. Kim, K. Singha, W.J. Kim, Transfection and intracellular trafficking properties of carbon dot-gold nanoparticle molecular assembly conjugated with PEI-pDNA, *Biomaterials* 34 (29) (2013) 7168–7180.
- [35] Z. Zhai, X. Qu, H. Li, Z. Ouyang, W. Yan, G. Liu, X. Liu, Q. Fan, T. Tang, K. Dai, A. Qin, Inhibition of MDA-MB-231 breast cancer cell migration and invasion activity by andrographolide via suppression of nuclear factor-kappaB-dependent matrix metalloproteinase-9 expression, *Mol. Med. Rep.* 11 (2) (2015) 1139–1145.
- [36] J. Liu, Y. Lu, Preparation of aptamer-linked gold nanoparticle purple aggregates for colorimetric sensing of analytes, *Nat. Protoc.* 1 (1) (2006) 246–252.
- [37] M.W. Roomi, J.C. Monterrey, T. Kalinovsky, M. Rath, A. Niedzwiecki, Patterns of MMP-2 and MMP-9 expression in human cancer cell lines, *Oncol. Rep.* 21 (5) (2009) 1323–1333.
- [38] W.J. Akers, B. Xu, H. Lee, G.P. Sudlow, G.B. Fields, S. Achilefu, W.B. Edwards, Detection of MMP-2 and MMP-9 activity *in vivo* with a triple-helical peptide optical probe, *Bioconjugate Chem.* 23 (3) (2012) 656–663.
- [39] J. Levi, S.R. Kothapalli, S. Bohndiek, J.K. Yoon, A. Dragulescu-Andrasi, C. Nielsen, A. Tisma, S. Bodapati, G. Gowrishankar, X. Yan, C. Chan, D. Starcevic, S. S. Gambhir, Molecular photoacoustic imaging of follicular thyroid carcinoma, *Clin. Cancer Res.* 19 (6) (2013) 1494–1502.
- [40] J. Yang, Z. Zhang, J. Lin, J. Lu, B.F. Liu, S. Zeng, Q. Luo, Detection of MMP activity in living cells by a genetically encoded surface-displayed FRET sensor, *Biochim. Biophys. Acta* 1773 (3) (2007) 400–407.
- [41] C. Moore, R.M. Borum, Y. Mantri, M. Xu, P. Fajtova, A.J. O'Donoghue, J.V. Jokerst, Activatable carbocyanine dimers for photoacoustic and fluorescent detection of protease activity, *ACS Sens.* 6 (6) (2021) 2356–2365.



Jinhwan Kim: Dr. Jinhwan Kim is a postdoctoral research scientist in the Wallace H. Coulter Department of Biomedical Engineering and the School of Electrical and Computer Engineering at the Georgia Institute of Technology. His research mainly focuses on implementing nanotechnology and exploiting nanomaterials' functionalities for clinical translation. Specifically, he designs nanosensors to enable real-time imaging of the pathogenic biomolecules in a noninvasive manner. In addition, he aims to track nanoparticle-modified cells *in vivo* via combined ultrasound and photoacoustic imaging.



Anthony M. Yu: Anthony Yu is a graduate student in the Wallace H. Coulter Department of Biomedical Engineering at the Georgia Institute of Technology and Emory University. His research focuses on employing tomographic photoacoustic, ultrasound, and fluorescence imaging techniques in combination with nanoagents for a range of diagnostic applications. These include the detection of early metastasis in breast and skin cancers and studying the development of vasculature in response to bioscaffold implantation.



Kelsey P. Kubelick: Dr. Kelsey Kubelick is in the Wallace H. Coulter Department of Biomedical Engineering and the School of Electrical and Computer Engineering at the Georgia Institute of Technology and Emory University. Her primary research focuses on development of cell and particle tracking approaches using ultrasound, photoacoustic, and magnetic resonance imaging to expedite translation of novel therapies, particularly in the fields of regenerative medicine and immunology. In addition, Kelsey is heavily engaged in medical device development for resource-limited environments to address pressing global health needs.



Stanislav Y. Emelianov: Dr. Stanislav Emelianov is a Joseph M. Pettit Endowed Chair, Georgia Research Alliance Eminent Scholar, and Professor of Electrical & Computer Engineering and Biomedical Engineering at the Georgia Institute of Technology and Emory University School of Medicine. Furthermore, Dr. Emelianov is Director of the Ultrasound Imaging and Therapeutics Research Laboratory. Projects in Dr. Emelianov's laboratory are focused on the discovery, development, and clinical translation of diagnostic imaging and therapeutic instrumentation, augmented with theranostic nanoagents.